Vol. 4, No. 2, May. 2005, pp. 169-192 ISSN: 1530-6429

Comparison of Numerical Methods for the Computation of Energy Spectra in 2D Turbulence. Part I: Direct Methods

Ch.H. Bruneau, P. Fischer, Z. Peter, A. Yger
Institut de Mathématiques de Bordeaux, Université Bordeaux 1
351 cours de la Libération
33405 Talence France
bruneau@math.u-bordeaux.fr

Abstract

The widely accepted theory of two-dimensional turbulence predicts a direct enstrophy cascade with an energy spectrum that behaves in terms of the frequency range k as k^{-3} and an inverse energy cascade with a $k^{-5/3}$ decay. However, the graphic representation of the energy spectrum (even its shape) is closely related to the tool which is used to perform the numerical computation. With the same initial flow, eventually treated thanks to different tools such as wavelet decompositions or POD representations, the energy spectra are computed using direct various methods: FFT, auto-covariance function, auto regressive model, and wavelet transform. Numerical results are compared to each other and confronted with theoretical predictions. In a forthcoming part II some adaptative methods combined with the above direct ones will be developed.

Key words and phrases: time-series analysis, power spectra, auto correlation, wavelets decomposition, auto regressive methods, proper orthogonal decomposition, wavelet and cosine packets.

2000 AMS Mathematics Subject Classification — 94A12, 62M10

1 Introduction

The study of two-dimensional turbulence theory was initiated by Kolmogorov [16, 17], Batchelor [3], and Kraichnan [18]-[20]. The theoretical prediction of two inertial ranges is a consequence of both energy and enstrophy conservation laws in the two-dimensional Navier-Stokes (NS) equations. Observing these two ranges in numerical or physical experiments remains a still up-to-date challenge within the frame of turbulence studies.

It follows from the works of Kraichnan and Batchelor that a local cascade of enstrophy from the injection scale to the smaller scales leads to a value of -3 for the slope in the representation of the logarithm of the energy spectrum in terms of the logarithm of the wave number. According to Saffman [32], the dominant contribution in the energy spectrum comes from effects resulting from the discontinuities of

vorticity. The value of the slope is then predicted to be -4. However, the rough value that is obtained by numerical simulations is in general located between these two theoretical values. Vassilicos and Hunt [37] demonstrated that accumulating spirals above vortices make the flow more singular so that the slope is attenuated down to the value of -5/3. The creation of vorticity filaments leading to these accumulating spirals occurs during the vortices merging process [15]. This process transfers energy to larger scales, thus creating the inverse energy cascade. The overall energy spectrum is depicted in Figure 1. While several numerical simulations and experiments have shown results, which agree in some relative way the theoretical predictions, few have really materialised the coexistence of both cascades [21, 6, 34, 35]. The experiment by Rutgers [31], using fast flowing soap films, remains one among such few realisations.

Starting from Direct Numerical Simulations (DNS) of Navier-Stokes (NS) equations that reveal the coexistence of both slopes, the main goal of this paper is to point out the difficulties encountered when analysing the results. Indeed, most of the methods are very sensitive to the various parameters and thus the same method can lead to significantly different results according to the choice of the parameters. Therefore, for each method we specify the adequate range of values to obtain relevant results.

We consider the flow behind an array of cylinders in a channel with rows of small cylinders along the vertical edges of the channel (Figure 2). We will compare numerical methods (based on Fourier, wavelets, and/or statistical models) that one can use to materialise (and then compute) energy spectra from numerical data (Section 3). The section 4 will be devoted to decomposition/reconstruction methods based on the Karhunen-Loeve [24, 33] decomposition and cosine or wavelet packets. In the forthcoming part II such decomposition/reconstruction methods will be combined with a matching pursuit algorithm [26]. A complementary study of two-dimensional turbulence based on the velocity and the vorticity analysis will be addressed in another publication. Those interested in two-dimensional turbulence theory should refer to Lesieur [22], Frisch [10], or Tabeling [36] for a complete overview on the topic.

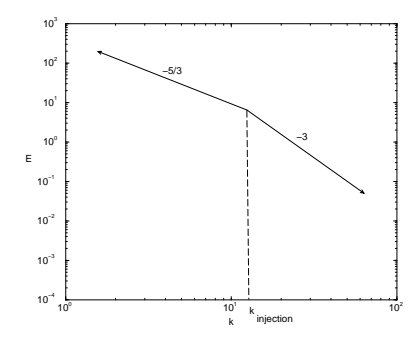


Figure 1: Theoretical spectrum cascades in 2D turbulence

2 Description of the experiments and numerical results

The numerical simulation of a two-dimensional channel flow perturbed by arrays of cylindersis performed, as shown in Figure 2. The length of the channel Ω is four times its width L; the Reynolds number based on the diameter of the bigger cylinders (equal to $0.1 \times L$) is Re = 50000.

The experiment consists in solving numerically the NS/Brinkman model described below (1) in $\Omega = \overline{\Omega_s} \cup \Omega_f$ where Ω_s (the "obstacle" subset) is the union of the five horizontal disks together with 18 small disks (with diameter equal to $0.05 \times L$) and Ω_f is the fluid domain as shown on Figure 2.

The evolutions in time of the velocity (two components), of the vorticity, and of the pressure have been recorded at a monitoring point located at $(x_1 = 3L/8, x_2 =$ 13L/16) sufficiently far away from the horizontal cylinders to take into account the developed turbulent events. These 1D temporal signals are then analysed and used to compute the energy spectra.

Numerical results obtained through such DNS can be compared to those obtained in the experiments realised thanks to physical devices by Hamid Kellay in [7]: a soap film in a rectangular channel is disturbed by five big cylinders together with two rows of smaller cylinders.

Let Ω_f be the fluid domain; its boundary is defined by $\partial \Omega_f = \partial \Omega_s \cup \Gamma_D \cup \Gamma_W \cup \Gamma_N$ (see Figure 2). A non-homogeneous Poiseuille flow is imposed on the boundary Γ_D as well as a no-slip boundary condition is imposed on the pieces of the boundary Γ_W . The obstacles are taken into account by a penalisation procedure that adds a mass term in the equations, which are now specified on the whole domain Ω as in [2]. Thus, we are looking for the solution of the following initial boundary value problem:

$$\partial_t U + (U \cdot \nabla)U - \operatorname{div} \sigma(U, p) + \frac{1}{K}U = 0 \text{ in } \Omega_T = \Omega \times (0, T)$$

$$\operatorname{div} U = 0 \text{ in } \Omega_T$$

$$U(\cdot, 0) = U_0 \text{ in } \Omega$$

$$U = U_D \text{ on } \Gamma_D \times (0, T)$$

$$U = 0 \text{ on } \Gamma_W \times (0, T)$$

$$\sigma(U, p) \cdot n + \frac{1}{2}(U \cdot n)^-(U - U^{ref}) = \sigma(U^{ref}, p^{ref}) \cdot n \text{ on } \Gamma_N$$

$$(1)$$

where $\sigma(U, p)$ is the stress tensor, U = (u, v) is the velocity vector, p is the pressure, U_0 is the initial datum, U_D the Poiseuille flow at the entrance section of the channel, U^{ref} and p^{ref} a reference flow used to write non-reflecting boundary conditions on the artificial exit section of the channel [8]. In this NS/Brinkman model, the scalar function K can be considered as the permeability of the porous medium.

Numerical simulations are performed on rectangular meshes $(1280 \times 320 \text{ or } 2560 \times$ 640 points) with a multi-grid approach. The two previous meshes correspond to grids 7 and 8, respectively. The time process lasts 40 units of non-dimensional time with a step of 10^{-3} leading to 40000 output data for each temporal signal (pressure,

components of the velocity, and vorticity) at the monitoring point in Ω_f . We see in Figure 3 that the velocity signals have roughly the same properties whereas the pressure and the vorticity signals exhibit huge picks corresponding to the convection of the coherent structures through the point position. In the following sections, the Taylor hypothesis is used to convert time scales to length scales. This hypothesis has been thoroughly tested in such flows [4] and assumes that the flow structures are convected through the monitoring point without much deformation.

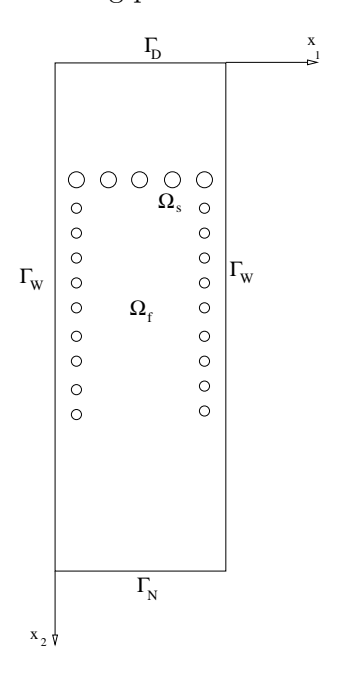


Figure 2: Computational domain

3 Energy spectrum computation

3.1 The basic FFT method

The simplest way to visualise the energy spectrum corresponding to a given signal consists in computing the power spectrum of the first component of the velocity u. We are allowed to consider only the transverse velocity component since the flow perturbations are mainly isotropic and thus the power spectral densities of both velocity components are essentially the same. So they represent correctly the energy spectrum. A first naïve attempt to perform such a computation has been done directly, applying the well-known discrete Fourier transform to the whole velocity signal. Although this signal is not periodic, a windowed version of the FFT method with functions such that Bartlett's or Hanning's is useless due to the large size of the signal. One can see immediately that graphical representations of the logarithms of the power spectra in terms of the logarithm of the wave number k (as represented on Figure 4 for the first component of the velocity signal) obtained

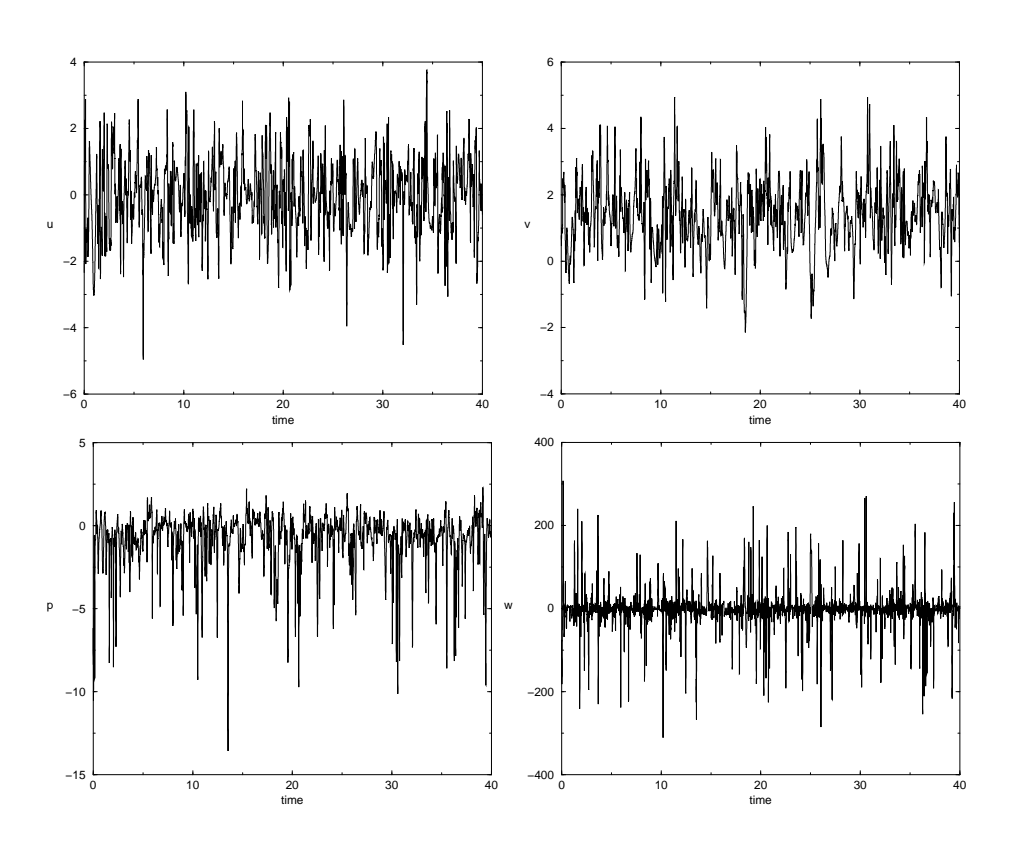


Figure 3: Signals of the physical quantities at the monitoring point

that way provide a very noisy graph. Despite the thick aspect of the graph, it is possible to determine the slopes of both cascades through a first order least square approximation. Their value fits more or less with the theoretical values.

One difficulty is the determination of the slope of the cascades as some parts of the spectrum have no physical or numerical meaning; namely, the frequencies corresponding to a size bigger than the channel width and the frequencies corresponding to the unresolved scales. Let the unity be the channel width; then the diameter of the horizontal cylinders is $\frac{1}{10}$. Due to that scaling, $k \approx 10$ is the main frequency of injection. The diameter of the smaller cylinders in the two vertical arrays is $\frac{1}{20}$, which corresponds to an injection frequency of $k \approx 20$. Moreover, the numerical simulation is performed on an uniform grid of mesh size $h = \frac{1}{320}$ or $h = \frac{1}{640}$. Assuming that for the representation of an oscillation generally we need 4 or 5 points, we expect to obtain significant scales between the wave numbers corresponding to the half size of the channel k = 2 and $k = \frac{1}{5h}$ or $k = \frac{1}{4h}$. Thus, it should be possible to determine correctly the two cascade slopes as following:

- for the *inverse cascade* (sl 1) between the frequencies k=2 and k=10
- for the enstrophy cascade (sl 2) between the frequencies 10 and $k = \frac{1}{5h}$ or $k = \frac{1}{4h}$.

To confirm this assumption we perform numerous slopes computation on the energy spectrum obtained from simulation grids 7 $(h = \frac{1}{320})$ and 8 $(h = \frac{1}{640})$. In the Figure 5 the enstrophy cascade slopes (on the vertical axis) are determined always between the wave number k = 10 and the wave numbers represented in the horizontal axis. We can observe an almost constant behaviour in the vicinity of the wave number k = 65, while the first part of the curve is due to the influence of the injection scales and the last part is due to the dissipative tail. The same slopes computation for $h = \frac{1}{640}$ gives the same behaviour with an almost constant value around k = 130. This fact shows that by increasing the numerical simulation of the flow by a factor 2, we double the range of the enstrophy cascade. However, due to the thickness of the energy spectra, an accurate estimation of the slope is quite difficult to obtain.

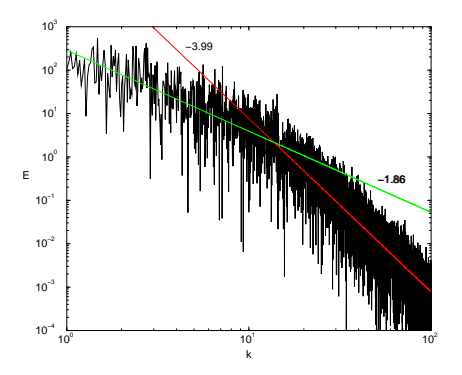


Figure 4: Energy spectrum obtained for the first component of the velocity with Fourier method

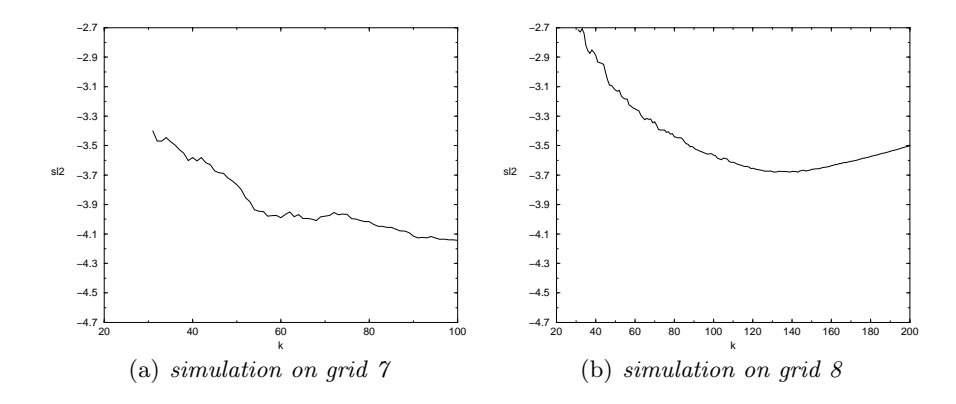


Figure 5: Determination of the upper bound to evaluate the enstrophy cascade slope

3.2The periodogram method

In order to overcome the difficulty arising in this naïve approach, one can combine it with statistical ideas by computing the discrete Fourier transform of the digital signals [s(l),...,s(l+p-1)] for l=1:q:40000-p and averaging the graphic representations obtained for the logarithm of the energy spectrum. We still treat the first component of the velocity. The graphical representations obtained from the Bartlett windowed Fast Fourier Transform algorithm with the window size p = 2048and the translation step q=8 are plotted in Figure 6. Note that the thickness of the energy spectra is drastically attenuated, though the time-frequency information is of course lost since one uses a statistical process. Of course, when the size p of the window increases up to the size of the signal, one recovers the thick energy spectra plotted in Figure 4.

Figure 7 shows the evolution of the estimated slopes with respect to the size p(between 10^3 and the extreme value 39×10^3) of the window when q is kept equal to 10. The slope within the inverse cascade range remains essentially located around -1.8, while the slope within the enstrophy cascade range takes values around -4, as in the previous subsection.

Let us point out to the reader that when the size p of the window is small it is necessary to use windowed Fast Fourier Transform to reduce the effect of the side lobs that introduce high frequencies and so modify the slope in the high frequency part of the spectrum. This is illustrated in Figure 8 where the slopes of the spectra obtained without windowing are about the same than those of Figure 7 except for small sizes $p \leq 10000$ in the enstrophy cascade.

3.3 The correlation method

One can determine the power spectral density of a signal as being the Fourier transform of the auto-covariance function. By the indirect (or the Blackman-Tukey) method, in a first stage one estimates the auto-covariance function and then, by taking the Bartlett windowed Fourier transform of this function, one calculates the

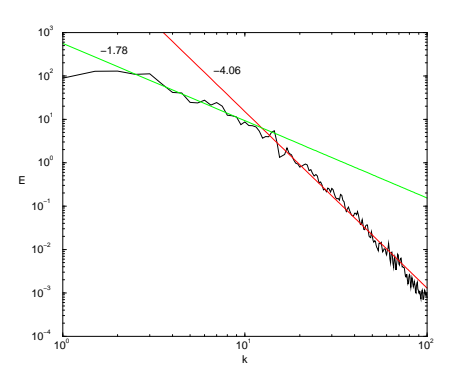


Figure 6: Energy spectrum obtained by the periodogram method with p=2048 and q=8 for the first component of the velocity

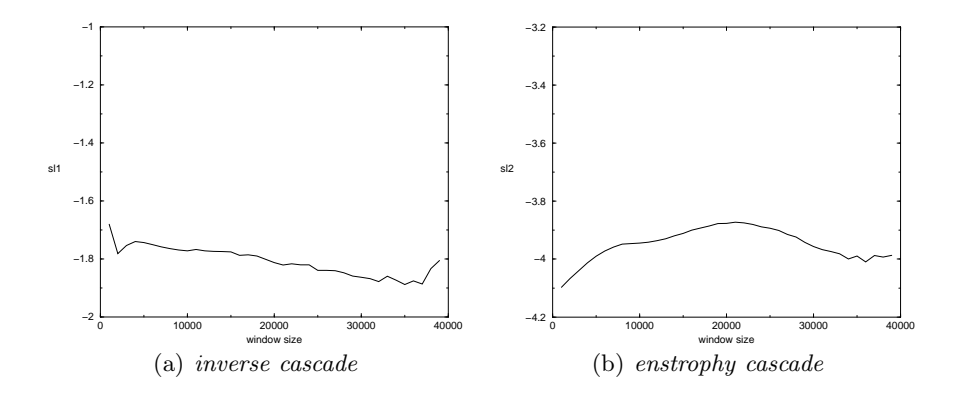


Figure 7: Evolution of the slopes in terms of the size of the window with the Bartlett windowed periodogram method

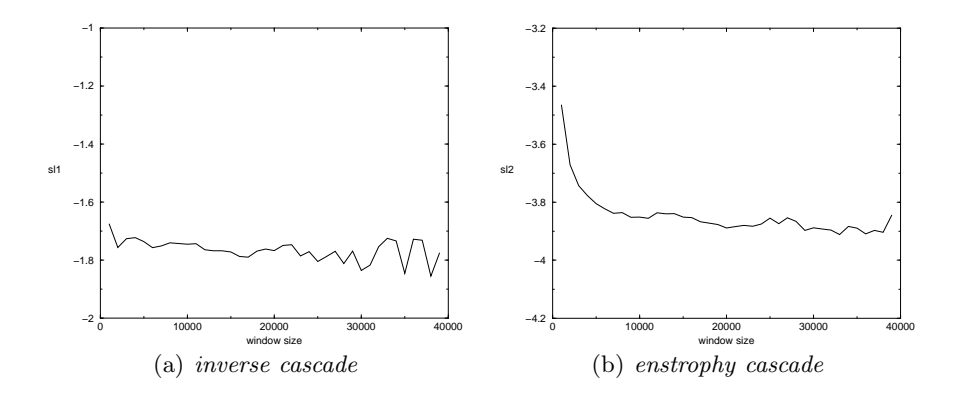


Figure 8: Evolution of the slopes in terms of the size of the window with the periodogram method

power spectral density. Let x_n , (n = 0, 1, 2..., N-1) be the studied signal containing N samples. A biased estimate of the auto-covariance function is given by

$$\widetilde{R}(Q) = \frac{1}{N} \sum_{n=0}^{N-Q-1} x_{n+Q} x_n \quad \text{with} \quad Q = 0, 1, \dots, N-1.$$
 (2)

The values of this function for the negative arguments can be deduced, beginning with the estimates obtained for the positive arguments by the relation

$$\widetilde{R}(-Q) = \widetilde{R}(Q). \tag{3}$$

In our case, N = 40000 and we will calculate the power spectral density of the signal using $M \leq N$ correlation coefficients. The results obtained for the energy spectrum for the first component of the velocity are displayed in Figure 9. When M is small the slopes are underestimated with an error up to 14\%, whereas the results are coherent with those obtained in the previous subsections for $M \geq 10000$. In Figure 10 we represent on the vertical axis the various values of the slopes for the variation of the correlation coefficients in the auto-covariance method. One can see the decreasing behaviour, especially on the level of enstrophy cascade, while the slope of the inverse cascade remains roughly unchanged except for M = 1000. These graphs can justify the choice of the needed correlation coefficients in the calculation of the slopes of the power spectrum. An insufficient number of coefficients can yield more than 10% of error. However, in this computation the choice of the windowing function is very important as the same study with Hanning function gives much better results, especially for the direct cascade.

Like in the periodogram, we can calculate the power spectral densities on some smaller windows and, taking the mean, obtain the estimated energy spectra (Welch method with no overlaps). Let x_n , (n = 0, 1, 2..., N - 1) be a digital signal (interpreted as a stationary process) with length N, we choose a window size p. Let us set the number of parameters M = E[p/2]; an unbiased estimate for the auto covariance function is given by

$$k \in \{0, ..., M-1\} \rightarrow \frac{1}{p} \operatorname{average}_n \left[\sum_{l=0}^{p-1-k} x_{n \times p+l+k} x_{n \times p+l} \right],$$

where the averaging process is taken over values of n between 0 and E[N/p]. In Figure 11 the results obtained with 20 windows of length 2000 are pridicted. For each such window we determine 1000 correlation coefficients and then the estimation of the energy spectrum is obtained by taking the mean of the power spectral densities. Here again the results are not correct as the size of the window is too small. Indeed, the estimated slopes obtained when one interprets energy spectra as power spectral densities of stationary processes depend on the value of the size p. Figure 12 shows the evolution of the two estimated slopes in terms of the value of such a size p when p increases from 1000 up to 20000. Once again a size at least p > 5000 is required to obtain reliable results. This is coherent with the fact that the validity of the correlation method lies on the assumption that the signal remains stationary on

windows of size p. Indeed, we can check the correlation matrix given in Figure 13 such that the stationary assumption is much more fulfilled for p = 20000 than for p = 1000.

In conclusion, there is a significant variation of the slopes with respect to the size p of the window that is used to compute the auto correlation. Relatively large values of p better verify that the stationary assumption holds and thus that the resulting slope is in very good accordance with the slopes obtained with the periodogram method in subsection 3.2.

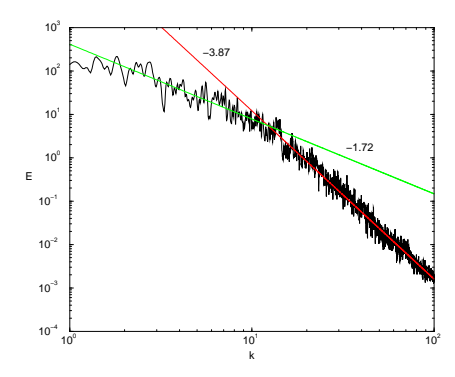


Figure 9: Energy spectrum obtained by the correlation method

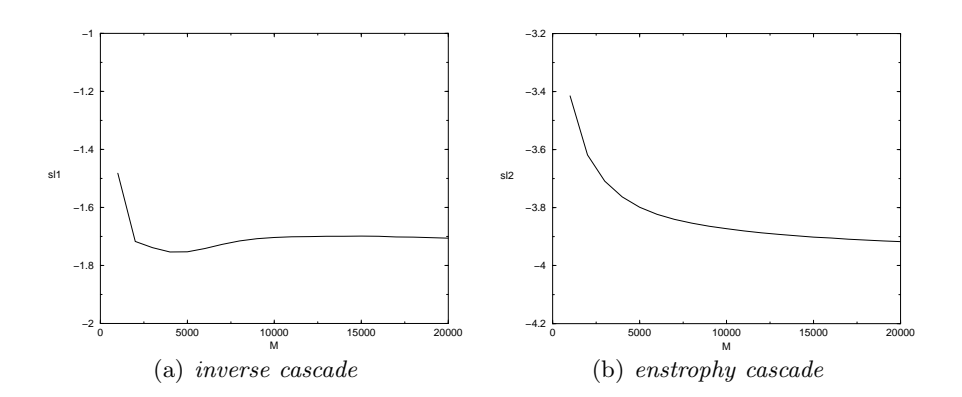


Figure 10: Slope estimates computed with the correlation method in terms of M

3.4 The method based on the auto regressive model

Let us consider again the digital real signal $(x_n)_n$, n = 0, ..., N - 1, corresponding, for example, to the measurements of the first component of the velocity, as a discrete stationary process. The search for an optimal auto regressive model with an *a priori* prescribed number of parameters (m < N) contains the determination of estimators

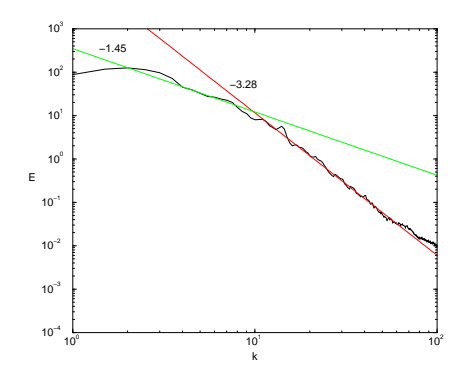


Figure 11: Cascades slopes computed with the correlation method using Welch method with 20 non overlapping windows of size p = 2000

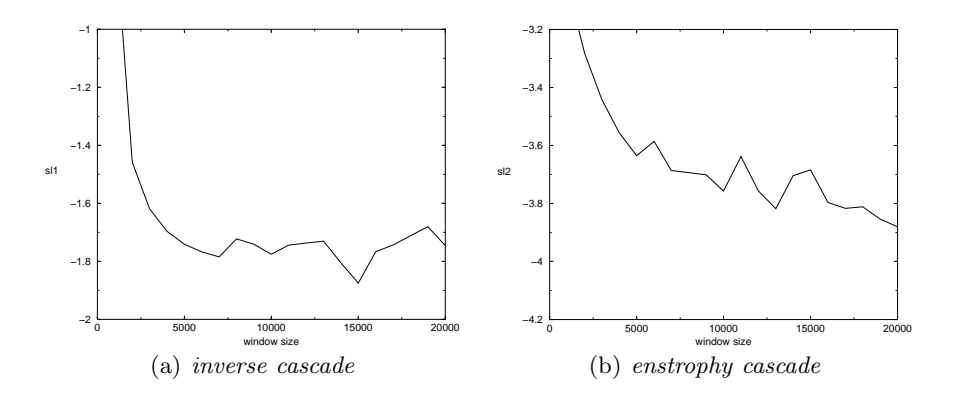


Figure 12: Slope estimates computed with the Welch correlation method in terms of the window size

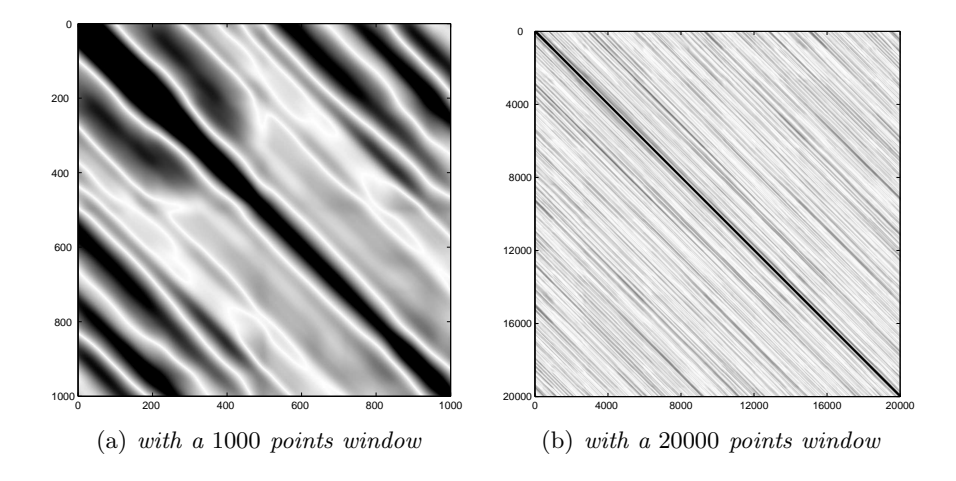


Figure 13: The correlation matrices for different time windows calculated for the first component of the velocity

 $\mu, \alpha_1, ..., \alpha_m$ such that

$$S(\mu, \alpha_1, ..., \alpha_m) := \sum_{n=m+1}^{N} z_n^2$$

$$= \sum_{n=m+1}^{N} \left[(x_n - \mu) - \alpha_1 (x_{n-1} - \mu) - \dots - \alpha_m (x_{n-m} - \mu) \right]^2$$

is minimal. In order to seek such estimators, the use of the least squares criterion takes its justification from the a priori assumption that the residual process

$$z_n := (x_n - \mu) - \sum_{l=1}^m \alpha_l(x_{n-l} - \mu), \quad n = m, ..., N - 1,$$
(4)

is Gaussian with mean value 0 and variance σ_z^2 , which means that μ corresponds essentially to the mean value of the digital process. Optimal values $\widehat{\alpha_1},...,\widehat{\alpha_m}$ for the coefficients $\alpha_1,...,\alpha_m$ are then computed through the Yule-Walker method [30, 14], and the corresponding numerical model for the power spectral density of the stationary process realised by the digital signal $(x_n)_n$ is

$$\omega \in [0, \pi] \to S_{xx}(\omega) = \frac{s_z^2}{|1 - \widehat{\alpha_1} \exp(-i\omega) - \dots - \widehat{\alpha_m} \exp(-im\omega)|^2},$$
 (5)

where s_z^2 denotes an unbiased estimate for the residual variance σ_z^2 , obtained when m << N as

$$s_z^2 = \frac{N - m}{N - 2m - 1} \left(\widehat{R}(0) - \sum_{l=1}^m \widehat{\alpha}_l \, \widehat{R}(l) \right), \tag{6}$$

 \widehat{R} being the auto covariance function of the digital process $(x_n)_n$, that is

$$\widehat{R}(l) := \frac{1}{N} \sum_{n=m}^{N-1} (x_n - \overline{x})(x_{n-l} - \overline{x}), \ l = 0, ..., m,$$

where \overline{x} denotes the mean value of $(x_n)_n$. The number of parameters must be carefully chosen since it highly influences the results. If this number is too low, the algorithm suppresses frequency peaks and does not allow a precise frequencies determination. If the number of parameters is too high, the method becomes very sensitive to the signal-to-noise ratio, and a number of artificial and irrelevant frequencies appear in the spectrum. If one applies this method to the digital velocity signals treated before, one obtains smooth representations of the logarithm of energy spectra as functions of the wave number. The frequency set $[0, \pi]$ is rescaled such that the graphics thus obtained fit with those which were obtained in the two previous subsections.

It is underlined in [38] that auto regressive methods provide good results when the filter length is of the same order than the number of samples per period (m =

1000 in our case). In Figure 14 we can see that the spectra calculated with a low number of auto regressive parameters is more smooth than the spectrum calculated with many more parameters. In the second case, a breakdown is observed around k=10 and so the determination of the slopes is easier. The same results are obtained with m = 1000 parameters except the curve is more oscillating. As soon as the number of parameters is large enough, the results are consistent with those obtained in the previous sections. However, various methods dealing with the detection of the optimal number of parameters were tested but did not give reliable results.

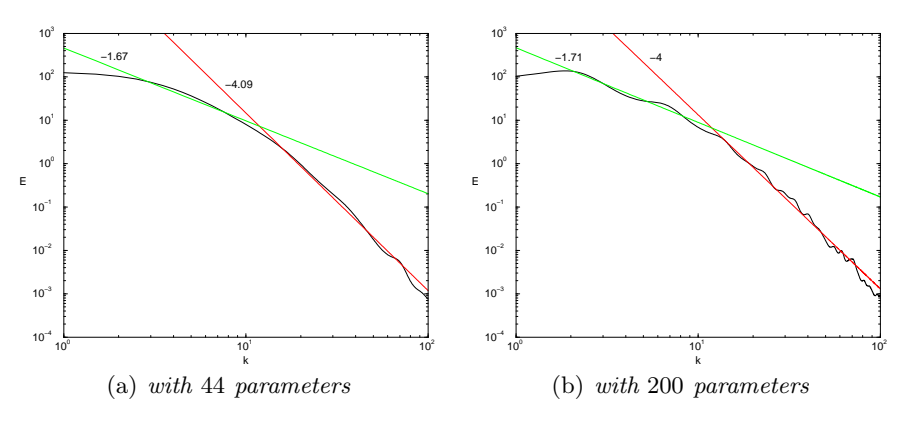


Figure 14: Energy spectra obtained by the autoregressive method with different parameters

3.5 Wavelet based spectrum

Wavelet decomposition is the realization of a decomposition of the input signal s into successive details d_i , j = 1, ..., k, plus an approximation r_k :

$$s = d_1 + d_2 + \dots + d_k + r_k. \tag{7}$$

Such a decomposition is obtained performing orthogonal projections of s on subspaces W_j generated by the functions $\psi(\frac{t-l}{2^j})$, $j \leq k$ for the details and on subspaces V_k generated by functions $\varphi(\frac{t-l}{2^k})$ for the resumed version r_k . The wavelet ψ is the mother of the corresponding multiresolution analysis interpreted as a pass-band filter while φ , which plays the role of a low-band filter, is the father of the corresponding multiresolution analysis.

Wavelet spectral densities are additive contributions to the total energy of the signal in a Plancherel-like identity

$$||s||^2 = ||d_1||^2 + ||d_2||^2 + \dots + ||d_k||^2 + ||r_k||^2,$$
 (8)

where $\|.\|$ denotes the l^2 discrete norm.

The wavelet based spectrum obtained for Daubechies 10 wavelet is shown in Figure 15. We can remark on the best quality fit of the spectra and the calculated slopes, which have similar values as in the other methods. The wavelet analysis depends on both the signal under study and the choice of the wavelet basis. For

a complete presentation of the now classical multiresolution analysis and wavelet theory, refer for example to [25], and for a detailed theoretical and numerical comparison between wavelet and Fourier spectra see the paper of Perrier, Philipovitch and Basdevant [28].

It has been stated in [28] that "the behaviour of the wavelet spectrum at large wave numbers depends strongly on the behaviour of the analysing wavelet at small wave numbers." This feature has been observed in our spectra, given in Figure 16, where the number of vanishing moments of the mother wavelet slightly modifies the slope of the spectra at large wave numbers can be observed. The obtained slope values are summarised in Table 1.

To conclude this section, it can be said that the four methods described here lead to results that are essentially similar. However, one must be very cautious as all the methods are very sensitive to their parameters. For instance, we have found a slope for the direct enstrophy cascade close to -4 but with some choices of the parameters it would be possible to get a slope close to -3 in order to be consistent with the two-dimensional turbulence theory. The results found in the literature often make evident one of the two slopes but rarely both of them within the same experiment [7].

Note that the method based on the wavelet decomposition provides the best representation in terms of smoothness for the energy spectrum.

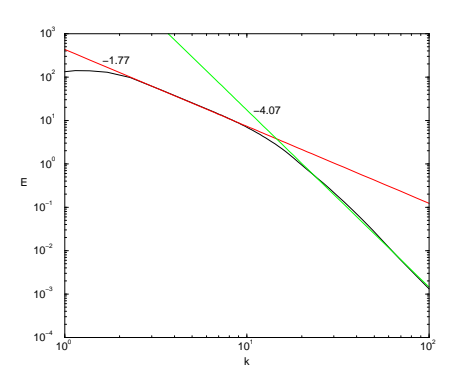


Figure 15: Energy spectra calculated with the wavelet based method using Daubechies10 wavelet

Wavelet type	Enstrophy cascade slope	Inverse cascade slope
Daubechies4	-3.94	-1.74
Daubechies10	-4.07	-1.77
Daubechies20	-4.11	-1.78

Table 1: Slopes obtained with different Daubechies type wavelets by wavelet based spectra calculation

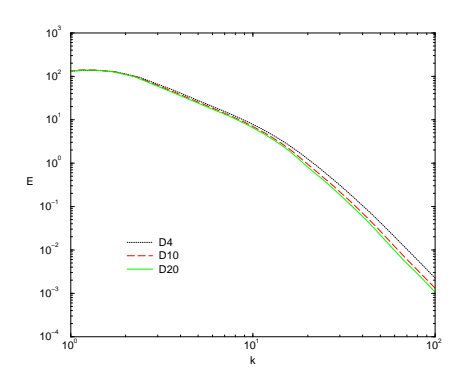


Figure 16: Spectra calculated with the wavelet based method using different Daubechies wavelets

Methods of decomposition – reconstruction 4

In this section, we compare different method of decompositions. Some of them take into account the signal itself like proper orthogonal decomposition. The decompositions of other ones, e.g., wavelet packets or cosine packets, lie on a systematic use of entropy criteria leading to the construction of the best basis.

Proper orthogonal decomposition (POD) 4.1

The POD, also called Karhunen-Loeve decomposition [24], is a classical method developed in statistics. Given a random process U, the overall algorithm can be summarised as follows:

- 1. Compute the auto-correlation matrix A of a set of realisations (also called "snapshots") of $U, U_1, ..., U_q$.
- 2. Perform the Singular Value Decomposition of A, thus organising the eigenvalues of A in decreasing order : $\lambda_1 \geq \lambda_2 \geq \cdots$.
- 3. Take $m \leq q$ and select an orthonormal (in the L^2 sense) system of vectors $(\alpha_{ij})_{1\leq i\leq q}, j=1,...,m$, such that $(\alpha_{ij})_i$ is an eigenvector respect to the eigenvalue λ_i .
- 4. Compute the POD modes

$$V_j := \sum_{i=1}^{q} \alpha_{ij} U_i, \quad j = 1, ..., m.$$

This four-step process provides the best basis for the set of realisations $\{U_1, ..., U_q\}$ work respect to the L^2 norm when m=q. Thus, given a random process, the effective implementation of the POD requires a set of realisations or snapshots. Instead of using several signals of length 40000 to create the set of snapshots, one will start from a given signal s (with length 40000), such as the registration of the vorticity,

the pressure, or one of the components of the velocity. We divide s(1:39936) in 39 consecutive non overlapping segments of length 1024. Each segment plays the role of a snapshot, thus leading to a dictionary \mathcal{D} of 39 snapshots and to an auto-correlation matrix of size 39×39 . The POD algorithm then provides 39 POD modes of length 1024, together with the coefficients one needs to rebuild each original segment as a linear combination of the proper modes. For example, the vorticity signal has been decomposed following this method and a few among the 39 proper modes multiplied by their corresponding eigenvalue are displayed in Figure 17.

One can also construct a collection of snapshots by breaking the original signal into overlapping segments with length 1024, thus leading to a redundant but richer set of realisations and therefore to a new family of proper modes [29]. The length of the segments used to realise snapshots can also be discussed since the quality of the reconstruction depends on it. Table 2 shows, for example, the number of POD modes that are necessary for the reconstruction, up to a given percentage of the initial L^2 norm, beginning with 156 consecutive non-overlapping segments of 256 points, 78 consecutive non-overlapping segments of 512 points, or 39 consecutive non-overlapping segments of 1024 points. In the following, we decide to use 39 snapshots as their length corresponds to the channel width for $\delta t = 10^{-3}$.

On the other hand, a dictionary of snapshots may be reduced without any significant effect on the efficiency of the atomic decomposition of a given signal s. This can be done introducing, for example, the following Variance Criterion (VC) used in [23]: a snapshot U_i remains within the dictionary provided its variance $(\sigma^{(i)})^2$ exceeds the variance σ_s^2 . For example, it can be seen in Figure 18 that from the original dictionary \mathcal{D} with 39 snapshots of 1024 introduced to analyse the vorticity signal, only 17 snapshots fit the criterion. The new dictionary contains only 17 snapshots U_i , which lead to the construction of 17 proper modes from an auto correlation matrix 17×17 . In fact, such a criterion allows us to reduce the dictionary of snapshots, keeping track of the shape of the POD modes corresponding to the most significant eigenvalues $\lambda_1, \lambda_2, \ldots$ One may check that the first POD modes obtained that way from the reduced dictionary of 39 snapshots with length 1024 are very similar to those corresponding to POD modes computed from the complete dictionary \mathcal{D} (Figure 17).

Subdivision	50%	99%
156×256	3	26
78×512	5	38
39×1024	6	33

Table 2: Number of POD modes necessary for the reconstruction of the signal with 50% and 99% the L^2 norm

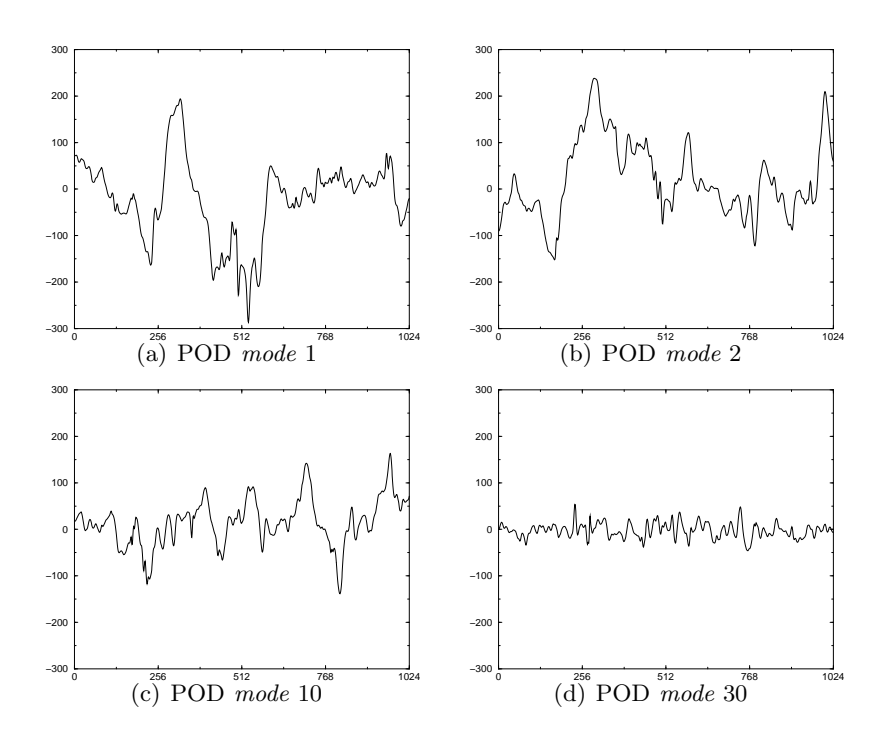


Figure 17: POD modes for the vorticity signal

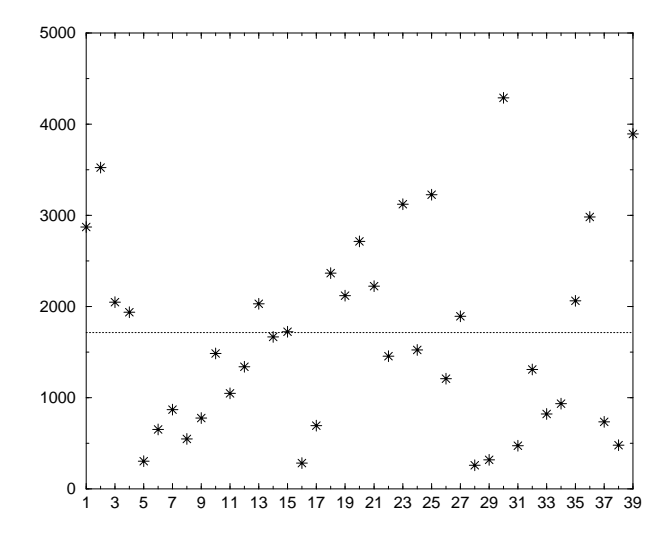


Figure 18: Variance of the representations U_i in \mathcal{D} compared to the variance of the signal (horizontal line)

4.2 Qualitative aspects of the reconstruction process coupled with the proper orthogonal decomposition

Any Proper Orthogonal Decomposition induces a reconstruction process. More precisely, if $(U_i)_{1 \leq i \leq q}$ are the snapshots and $V_1, ..., V_q$ the associated proper modes, we denote, for k = 1, ..., q, $U_{i,k}$ the orthogonal projection of U_i on the subspace generated by $V_1, ..., V_k$. The speed with which $\min_i(\|U_{ik}\|/\|U_i\|)$ converges to 1 when k increases is a good indicator of the quality of the POD with respect to the reconstruction of the snapshots. Such a speed also indicates the efficiency of the reconstruction process.

Since reconstructing the snapshots leads to a restitution of the signal, a proper orthogonal decomposition associated to such a segmentation is qualitatively efficient provided the signal can be approximately reconstructed from the least number of proper modes. In Figure 19, the evolution of the intermediate reconstruction ratio

$$r_k := \frac{\sum_{i=1}^{39} \|U_{ik}\|^2}{\|s\|^2}$$

is represented graphically as a function of k when $U_1, ..., U_{39}$ are the 39 snapshots of the dictionary \mathcal{D} . Note for instance that the first 5 modes representing about 13% of the total number of modes are sufficient to recover the original signal up to a relative energy of about 45%.

The reconstruction process does not behave equally well when applied to the restitution of a randomly chosen segment of the signal. Each segment of s can be modelled as a linear combination of the proper modes, which are enough to reconstruct the segment up to the best possible relative energy error. Note that there is no reasons to get the first proper modes as the most significant in the decomposition of the segment. Two segments S_1 and S_2 of length 1024 have been randomly chosen in the vorticity signal s and plotted in Figure 20. The respective reconstructions from the proper orthogonal decomposition attached to the dictionary \mathcal{D} are compared. Namely, the graphics of the functions:

$$k \to r_{1k} := \frac{\|\operatorname{pr}_{(V_1,\dots,V_k)}[S_1]\|^2}{\|S_1\|^2}$$

 $k \to r_{2k} := \frac{\|\operatorname{pr}_{(V_1,\dots,V_k)}[S_2]\|^2}{\|S_2\|^2}$

have been represented in Figure 21. The first evident fact is that the reconstruction process is more efficient when applied to S_1 than to S_2 . Indeed, to recover a relative energy of about 50%, 13 POD modes are requested for S_1 and all the POD modes for S_2 . Three reasons may explain such a crucial difference:

• The segment S_1 is more regular than the segment S_2 , which makes the reconstruction of S_1 with smooth signals such as the proper modes corresponding to the most significant eigenvalues easier than that of S_2 ;

- On the one hand, the support of the segment S_1 almost fits the support of a single snapshot, i.e., the 23^{rd} snapshot that starts at the 22529^{th} point. Most of the content of S_1 has been used to build the POD modes. On the other hand, the support of the segment S_2 overlaps significantly the supports of two snapshots (the 11^{th} and the 12^{th});
- The 23^{rd} snapshot has a variance which dominates the overall signal variance, while the 11^{th} and 12^{th} snapshots have variances lying below the overall signal variance. This implies that the segment S_1 corresponds to a dominating part within the signal, which is not the case for the segment S_2 .

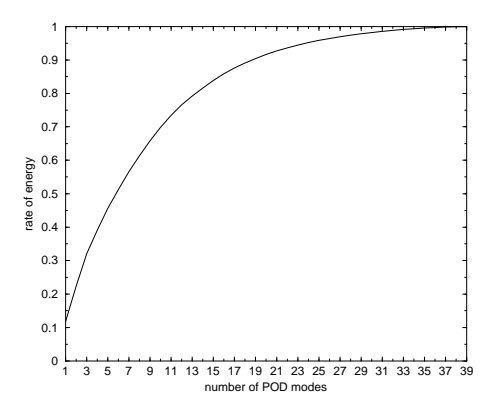


Figure 19: Quality of the reconstruction versus the number of POD modes

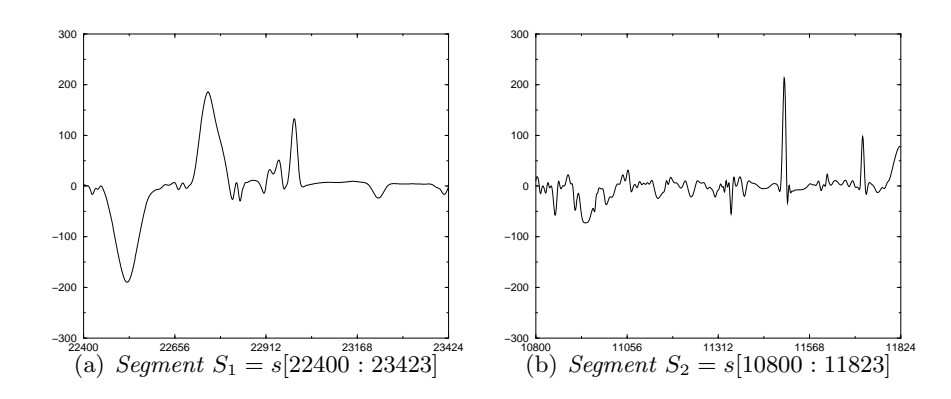


Figure 20: Randomly chosen segments of the vorticity signal

4.3 POD decomposition – reconstruction vs. numerical spectral analysis

Let s be the signal corresponding to the first component of the velocity and $\mathcal{D}_{\text{vel}} :=$ $\{U_i; i=1,...,39\}$ the dictionary of snapshots corresponding to non-overlapping segments with length 1024, with corresponding proper modes $V_1, ..., V_{39}$. For each k

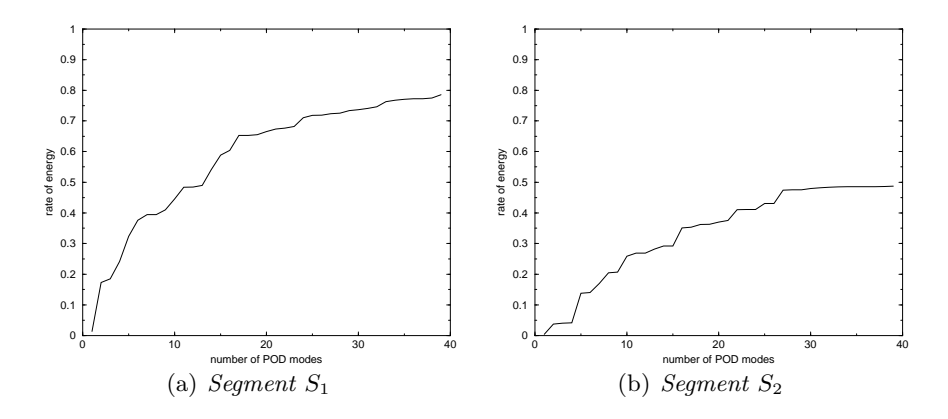


Figure 21: Quality of the reconstruction versus the number of POD modes

between 1 and 39, one computes the energy spectrum of the partially reconstructed signal using the basic FFT method described in section 3.1

$$s_k := [U_{1,k} \ U_{2,k} \ \cdots \ U_{i,k} \ \cdots \ U_{39,k}],$$

where $U_{i,k}$ denotes the orthogonal projection of U_i on the subspace $(V_1, ..., V_k)$. Then, for each s_k , the computation of estimated slopes for both cascades has been carried out. Results obtained for the evolution of the two estimated slopes in terms of k are quoted in Figure 22.

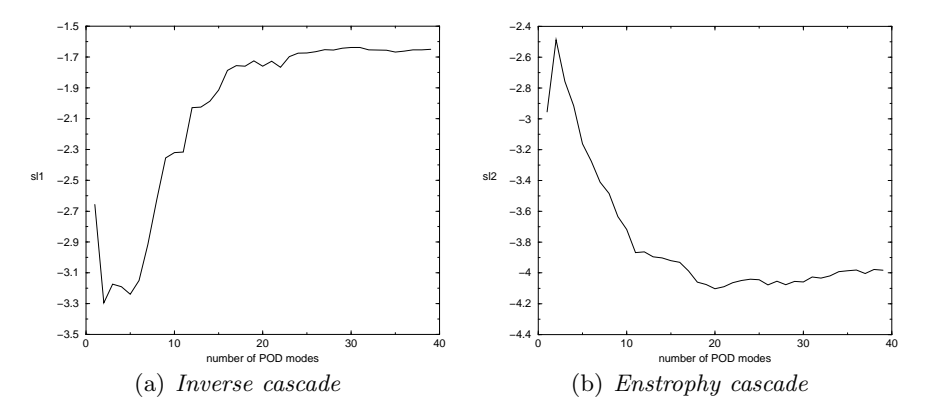


Figure 22: Evolution of the slopes in function of the number of POD modes in the reconstruction

4.4 Wavelet and cosine packets decompositions

Given a signal s and a multiresolution analysis, the associated splitting lemma leads to the selection of an orthonormal basis such that the Shannon entropy of s respect to its decomposition in such a basis is minimal. The elements of this kind of basis are wavelet packets; such functions generalise compactly-supported wavelets and constitute a redundant set of basis functions. In the same vein, the windowed Fourier transform induces through Malvar's decomposition the realisation

of a split and merge algorithm, which leads (still through an entropy criterion) to the construction of a best basis whose elements are cosine packets. More details about the theory, together with numerical tests based on various entropy criteria, can be found for example in [25, 39].

Wavelet packet decompositions are applied here to a signal (pressure, velocity, or vorticity at one of the monitoring points) truncated in order to have length 2^{15} . The Shannon entropy criterion governs the selection process of the best basis. Furthermore, a second entropy criterion is used in order to select significant components of s within its decomposition in such a basis (in order for example to recover the original signal up to a relative energy error less than 1%). Combining the best basis selection with this second entropy criterion leads to an approximated reconstruction of the given signal s also in terms of cosine packets atoms, which essentially look like rectangular windows times cosine functions. The energy spectrum of such an approximation models the energy spectrum of s. Table 3 indicates both the number of such atoms and the estimated values of the inverse and enstrophy cascades slopes for the corresponding approximation.

It is also important to test the efficiency of the reconstruction process on random segments of the signal. As for the POD reconstruction process, all segments do not behave equally. In Table 4, such efficiency has been tested on segments S_1 and S_2 . The number of atoms that are necessary to reconstruct S_2 up to a relative energy error less than 1% is at least three times the number of atoms one needs to reconstruct S_1 .

Basis type	# elements	enstrophy cascade	inverse cascade
Haar	1742	-3.10	-1.83
Daubechies6	910	-4.10	-1.82
Coiflet2	863	-4.23	-1.82
Symmlet8	766	-5.08	-1.81
Cosine	1147	-3.80	-1.80

Table 3: Number of elements necessary to reconstruct the signal up to 99% of the L^2 norm with the best basis algorithm and cascades slopes of the global reconstructed signal

Basis type	# elements for S_1	# elements for S_2
Haar	47	143
Daubechies6	22	121
Coiflet2	24	101
Symmlet8	21	100
Cosine	33	156

Table 4: Number of elements necessary to reconstruct signals S_1 and S_2 up to 99% of the L^2 norm with the best basis algorithm

5 Conclusions

Several conclusions can be drawn from this study on 2D turbulence. The shape of the spectra is in agreement with the theory and with the results generally obtained by other authors. The graphs are more or less thick depending on the method used to compute the spectra. The smoothest results have been obtained with the auto-regressive model and wavelet method.

Different methods of decomposition have also been studied: POD, wavelet, and cosine packets with the best basis algorithm. For the computation of the POD modes, the signal has been cut in several parts called snapshots. The method appears to be efficient for the analysis of one of the snapshots but reveals to be less adapted for a segment randomly chosen in the signal. On the contrary, the best basis algorithm in a frame of a wavelet or cosine packets decomposition can reconstruct any part of the signal with a reasonable number of elements. We shall see in the forthcoming part II how one can benefit of combining such methods towards an adaptative algorithm such as matching pursuit.

References

- [1] D.J. Acheson, Elementary fluid dynamics, Clarendon press, 1990.
- [2] Ph. Angot, C.H. Bruneau, P. Fabrie, A penalization method to take into account obstacles in incompressible viscous flow, Numer. Math. 81 n°4 497-520, 1999.
- [3] G.K. Batchelor, Computation of the energy spectrum in homogeneous twodimensional turbulence, Phys. Fluids 12 233-239, 1969.
- [4] A. Belmonte, B. Martin, W.I. Goldburg, Experimental study of Taylor's hypothesis in a turbulent soap film, Phys. Fluids 12 835-845, 2000.
- [5] J.P. Bonnet, J. Delville, Coherent structures in turbulent flows and numerical simulations approaches, Lecture Series 2002-04 von Karman Institute for Fluid Dynamics, 2002.
- [6] V. Borue, Inverse energy cascade in stationary two-dimensional homogeneous turbulence, Phys. Rev. Lett. **72** 1475-1478, 1994.
- [7] C.H. Bruneau, O. Greffier, H. Kellay, Numerical study of grid turbulence in two dimensions and comparison with experiments on turbulent soap films, Phys. Rev. E 60 R1162, 1999.
- [8] C.H. Bruneau, P. Fabrie, New efficient boundary conditions for incompressible Navier-Stokes equations: a well-posedness result, RAIRO Modél. Math. Anal. Numér. **30** n°7 815-840, 1996.
- [9] L. Cordier, M. Bergmann, Two typical applications of POD: coherent structures reduction and reduced order modeling, Lecture Series 2002-04 von Karman Institute for Fluid Dynamics, 2002.

- [10] U. Frisch, Turbulence, Cambridge University press, 1995.
- [11] Ph. Holmes, J.L. Lumley, G. Berkooz, *Turbulence, coherent structures, dynamical systems and symmetry* Cambridge University press, 1998.
- [12] A. Iollo, A. Dervieux, J.A. Désidéri, S. Lanteri, Two stable POD-based approximations to the Navier-Stokes equations, J. Comput. Vis. Sci. 3 n°1-2 61-66, 2000.
- [13] A. Iollo, S. Lanteri, J.A. Désidéri, Stability properties of POD-Galerkin approximations for the compressible Navier-Stokes equations, J. Theor. Comput. Fluid Dyn. 13 n°6 377-396, 2000.
- [14] Jenkins, M. Gwilym, Watts, G. Donald Spectral analysis and its applications, Holden-Day, 1968.
- [15] N.K Kevlahan, M. Farge, Vorticity filaments in two-dimensional turbulence: creation, stability and effect, J. Fluid Mech. **346** 49-76, 1997.
- [16] A.N. Kolmogorov, The local structure of turbulence in incompressible viscous fluid for very large Reynolds numbers, Dokl. Akad. Nauk. USSR **30** 301-305, 1941.
- [17] A.N. Kolmogorov, Dissipation of energy in locally isotropic turbulence, Dokl. Akad. Nauk. USSR **32** 16-18, 1941.
- [18] R.H. Kraichnan, *Inertial ranges transfer in two-dimensional turbulence*, Phys. Fluids **10** 1417-1423, 1967.
- [19] R.H. Kraichnan, Inertial-range transfer in two- and three-dimensional turbulence, J. Fluid Mech. 47 525-535, 1971.
- [20] R.H. Kraichnan, D. Montgomery, Two-dimensional turbulence, Rep. Prog. Phys. 43 547-619, 1980.
- [21] D.K. Lilly, Numerical simulation of developing and decaying two-dimensional turbulence, J. Fluid Mech. 45 395-415, 1971.
- [22] M. Lesieur, Turbulence in fluids stochastic and numerical modeling, Martinus Nijhoff publishers, 1987.
- [23] J. Liandrat, F. Moret-Bailly, The wavelet transform: Some applications to fluid dynamics and turbulence, Eur. J. Mech., B/Fluids 9 n°1 1-19, 1990.
- [24] M. Loeve, Probability theory, Van Nostrand, 1955.
- [25] S. Mallat, A wavelet tour of signal processing, Academic press, 1999.
- [26] S. Mallat, Z. Zhang, Matching pursuits with time-frequency dictionaries, IEEE Trans. Signal Process. 41 n°12 3397-3415, 1993.

- [27] A. Neumaier, T. Schneider, Estimation of parameters and eigenmodes of multivariate autoregressive models, ACM Trans. Math. Software 27 n°1 27-57, 2001.
- [28] V. Perrier, T. Philipovitch, C. Basdevant, Wavelet Spectra compared to Fourier Spectra, J. Math. Phys. 36(3), 1506-1519, 1995.
- [29] Z. Peter, Analyse de signaux et d'images en turbulence 2D, Ph D thesis, Université Bordeaux 1, 2004.
- [30] M.B. Priestley, Spectral analysis and time series. Volume 1: Univariate series. Volume 2: Multivariate series, prediction and control, Academic Press, 1981.
- [31] M.A. Rutgers, Forced 2D turbulence: experimental evidence of simultaneous inverse energy and forward enstrophy cascades, Phys. Rev. Lett. 81 2244-2247, 1998.
- [32] P.J. Saffman, Vortex Dynamics, Cambridge University Press, 1995.
- [33] L. Sirovich, Turbulence and the dynamics of coherent structures, Quarterly Appl. Math. 15 n°3 561-590, 1987.
- [34] L.M. Smith, V. Yakhot, Bose condensation and small-scale structure generation in a random force driven 2D turbulence, Phys. Rev. Lett. **71** 352-355, 1993.
- [35] L.M. Smith, V. Yakhot, Finite size effects in forced two-dimensional turbulence, J. Fluid Mech. 274 115-138, 1994.
- [36] P. Tabeling, Two-dimensional turbulence: a physicist approach, Phys. Rep. **362** 1-62, 2002.
- [37] J.C. Vassilicos, J.C. Hunt, Fractal dimensions and spectra of interfaces with application to turbulence, Proc. R. Soc. Lond. Ser. A 435, 505-534, 1991.
- [38] D. Veynante, Survey of signal processing techniques, Lecture Series 2002-04 von Karman Institute for Fluid Dynamics, 2002.
- [39] M.V. Wickerhauser, Adapted wavelet analysis from theory to software, Wellesley, A.K. Peters Ltd, 1994.
- [40] A. Yger, Théorie et analyse du signal. Cours et initiation pratique via MATLAB et SCILAB, Editions Ellipses, 2000.